Title

Nuclear biocondensate-forming lncRNA and cellular stress surveillance shape host cancer susceptibility

Anjali Bajpai[1,2*], Quazi Taushif Ahmad[1], Sushmita Kundu[1], Ravi Kant Pandey[1,3], Alan Goodman[4], Apul Goel[5], Bushra Ateeq[1,2], Subhash C. Lakhotia[6], Pradip Sinha[1,2]

[1]Biological Sciences and Bioengineering, Indian Institute of Technology Kanpur, Kanpur 208016, India.
[2]The Mehta Family Centre for Engineering in Medicine, Indian Institute of Technology Kanpur, Kanpur 208016, India.
[3]Current Address: PierianDx India Pvt Ltd, Chattushringi, Gokhalenagar, Pune 411016, Maharashtra, India
[4]School of Molecular Biosciences, College of Veterinary Medicine, Washington State University, Pullman, WA 99164, USA
[5]Department of Urology, King George's Medical University, Lucknow 226003, Uttar Pradesh, India.
[6]Cytogenetics Laboratory, Department of Zoology, Banaras Hindu University,Varanasi, 221005, India.
* Corresponding author: Anjali Bajpai, anjalii@iitk.ac.in

ORCID:
A. Bajpai: 0000-0002-5645-2466
B. Ateeq: 0000-0003-4682-9773
A. G. Goodman: 0000-0001-6394-332X
S. C. Lakhotia: 0000-0003-1842-8411
P. Sinha: 0000-0002-9202-6050

Running title: Host genetic regulators of cancer susceptibility

Key words

lncRNA *hsrω*, omega speckles, nuclear condensate, haploinsufficiency, proteostasis, tumor susceptibility, *dSTING*, *Keap1*

Abstract

Host genetics is known to influence cancer susceptibility. However, the specific candidate genes and molecular mechanisms that confer resistance remain poorly understood. Here, we demonstrate the power of haploinsufficiency screen to uncover host genetic regulators of cancer in *Drosophila* and identify the long noncoding RNA (lncRNA) *hsrω*, a structural component of nuclear biomolecular condensate known as omega speckles, as a key host cancer susceptibility locus. Loss of *hsrω* disrupts proteostasis and cell fitness, while its haploinsufficiency accelerates epithelial tumor progression driven by loss of the Lethal giant larvae (Lgl) tumor suppressor. Further validating the breadth of this screening strategy, we independently identified *Drosophila STING* (innate immunity) and *Keap1* (oxidative stress defense) as genetic modifiers of cancer. Moreover, in humans, copy number variations (CNV) in these genes and *Sat III* (a functional human homolog of *hsrω*) correlate with poor cancer prognosis, thereby revealing conserved stress pathways as potential host genetic susceptibility regulators.

Introduction

Genetic modifiers of cancer are genes that influence cancer risk by interacting with primary driver mutations or oncogenic processes without independently causing cancer. One of the central paradoxes of cancer biology is that, while a variety of oncogenes and tumor suppressors have been identified based on their causal underpinnings of cancer, modifier genes regulating host genetic susceptibility in humans remain underexplored (Castro-Giner et al., 2015; Turnbull et al., 2018). Among the known examples of host genetic modifiers identified by Genome-wide association studies (GWAS), notable are DNA repair genes for oxidative damage (*MUTYH* and *OGG1*, (Raetz and David, 2019), immune checkpoint genes (*CTLA4* and *PDCD1*, (Behrouzfar et al., 2021), or those affecting apoptosis pathways (*BIRC5*, (Siragusa et al., 2024). However, GWAS have limited capacity to identify functional cancer modifiers, which often require validation via haploinsufficiency or heterozygosity tests (Chenevix-Trench et al., 2007; Zeng et al., 2019). In *Drosophila*, genetic tractability enables a rapid assessment of such modifiers (Datta et al., 2023). A classic precedent is the *Minute* (Morata and Ripoll, 1975) class of ribosomal genes (Kongsuwan et al., 1985). Their haploinsufficiency compromises cellular proteostasis (Baumgartner et al., 2021) and disrupts tumor surveillance. Consequently, *Minute* +/- cells are outcompeted by fitter wild type cells or, conversely, fail to compete against tumors, thereby enhancing progression when tumor suppressors are lost (Agrawal et al., 1995; Froldi et al., 2010; Khan et al., 2013).

An emerging theme in cancer biology centres on the role of phase-separated biomolecular condensates, the dynamic cellular entities that regulate processes ranging from signalling and transcription to proteostasis and immune surveillance (Mehta and Zhang, 2022; Shin and Brangwynne, 2017). Disruptions of condensate integrity are increasingly linked to diverse pathologies including tumorigenesis (Banani et al., 2017; Boija et al., 2021). For instance, oncogene activation often utilizes super-enhancer condensates (Sabari et al., 2018) while the loss of PML condensates, for example, compromises p53 availability (Zhang et al., 2024).

In *Drosophila*, the long noncoding RNA-encoding *hsrω* gene codes for multiple transcripts ((Bendena et al., 1989; Lakhotia, 2011), also see **Figure 1A**), the largest nuclear-retained transcript, forms a scaffold for nucleoplasmic condensates known as omega speckles ((Prasanth et al., 2000), also see **Figure 1B**). These condensates dynamically sequester diverse heterogenous ribonuclear proteins (hnRNPs) and RNA-binding proteins (RBPs) to buffer cellular stress (Singh and Lakhotia, 2015). Crucially, loss of *hsrω* transcripts or the HRB87F hnRNP disrupts these condensates (Singh and Lakhotia, 2012). This biology is conserved since the functional human homolog, *Satellite III* (*Sat III*), similarly forms phase-separated nuclear stress bodies dependent on Heat shock factor 1 (HSF1) and sequester RNA-binding proteins (Goenka et al., 2016; Jolly et al., 2002; Jolly et al., 2004). Given the critical role of *hsrω* in stress buffering, we hypothesized that genetic perturbation of this lncRNA would profoundly impact cancer progression.

Here, we employed a hypothesis-driven candidate gene approach to uncover host genetic modifiers of cancer. We demonstrate that the omega speckle-associated lncRNA, *hsrω*, acts as a potent host genetic modifier of cancer susceptibility by regulating proteostasis. Furthermore, to validate the breadth of this haploinsufficiency screening approach, we expanded our search to other arms of the cellular stress response. We demonstrate that *Drosophila STING* (*dSTING*), a regulator of innate immune stress (Cai et al., 2020; Martin et al., 2018) and *Keap1*, a regulator of oxidative stress (Sykiotis and Bohmann, 2008) also serve as independent host genetic modifiers. Collectively, our findings highlight a conserved network of stress surveillance pathways that define tumor susceptibility.

Results

Study design

To systematically uncover how host genetics contributes to intrinsic epithelial tumor surveillance, we employed a candidate gene approach focusing on haploinsufficiency. We selected distinct but potentially overlapping stress regulators: the nuclear biomolecular condensate-associated lncRNA, *hsrω*, the innate immunity pathway component, *dSTING* and the redox regulator Keap1. Our strategy involved a stepwise characterization: first, we defined the consequences of *hsrω* loss on tissue growth, proteostasis, and cellular fitness in normal epithelium. Next, we tested whether *hsrω* haploinsufficiency facilitates the neoplastic transformation of somatic clones lacking the tumor suppressor *Lgl*. Finally, extending the logic of stress surveillance, we examined whether haploinsufficiency of *dSTING*—a key sentinel of the cGAS–STING pathway—mirrors the tumor-promoting effects of *hsrω* loss, thereby establishing a broader role for stress regulators in host cancer susceptibility.

hsrω mutants are growth-compromised and display disrupted proteostasis

Homozygosis for the *hsrω* near-null mutant, $hsr\omega^{66}$ (Johnson et al., 2009), causes high embryonic lethality, with the escapers emerging as weak short-lived adults . Analysis of these larvae revealed undergrown wing imaginal discs with significantly fewer dividing cells per unit

area than controls (**Figure 1C–F**) and elevated cell death (**Figure 1G, H**). The *hsrω*^{66} somatic clones were similarly smaller than their wild type twin spots, with cell death evident along clone borders (**Figure 1I, J**)—a phenotype characteristic of 'loser' cell behaviour in cell competition (de la Cova et al., 2004; Moreno et al., 2002). These growth defects prompted us to examine whether loss of *hsrω* perturbs the protein homeostasis landscape in developing epithelial cells.

Proteomic profiling revealed a collapse in the translation machinery. Comparing the proteome of mutant and wild type (WT) larval wing epithelium, we noted >±2-fold ($p<0.05$) changes in 73 proteins in *hsrω*^{66} mutants (**Figures 2A and S1A, B**). We observed a specific depletion of ribosomal structural proteins (RpS15Ab, mRpL50, and mRPL24; **Figure 2B**) alongside proteins involved in protein stability such as the heat shock protein Hsp23 and protein turnover, the SUMO-protease Ulp1 (**Figure S1C**). Rank-based enrichment analysis confirmed the overall downregulation of cytosolic and mitochondrial large ribosomal subunits (**Figure 2C**), as well as the cytoplasmic and mitochondrial translation machinery (**Figure 2D**). Furthermore, RNA Pol II transcription machinery components and the mediator complex were depleted (**Figures S1E**), indicating a systemic failure in gene expression and protein synthesis control. We noted that the *hsrω*^{66} proteome showed an upregulation of stress response markers (**Figure S1D**), including the cytoplasmic Glutathione S-transferase E6 (GstE6) (Aloke et al., 2024) and mitochondria-associated Mgstl (Toba and Aigaki, 2000)**,** indicative of redox imbalance. Such cellular changes likely prefigure DNA damage signatures, consistent with the observed elevation of Rpa1, a DNA double-strand break-associated protein (**Figures 2E**).
We further validated these proteomic signatures using cellular stress markers. The *hsrω*^{66} mutant wing epithelium displayed elevated ROS levels (DHE staining; **Figure 2F**) and enhanced JNK signaling (**Figure 2G**). This oxidative stress was accompanied by augmented γH2AX staining, confirming the presence of DNA double-strand breaks (Mah et al., 2010 ; **Figures 2H**). We reasoned that a suboptimal proteome under such stress would lead to the accumulation of damaged proteins, necessitating increased lysosomal clearance (Settembre et al., 2013). In agreement, *hsrω*^{66} wing discs showed increased acidic lysosomes detected by LysoTracker (**Figure 2I**) and an increase in Ubiquitin-positive foci (**Figure S2G**) indicating proteins marked for proteasomal degradation (Martínez-Férriz et al., 2022). Finally, we observed signatures of increased proteotoxicity in the wing epithelium owing to loss of proteostasis. For instance, the mutant proteome showed a marked elevation of ARC1 and ARC2 (**Figure 2A**), proteins associated with pathological aggregates (Schulz et al., 2023). Crucially, *hsrω*^{66} wing epithelium exhibited marked increase in cellular uptake of ProteoStat (**Figure 2J**), a dye that fluoresces upon intercalation with protein aggregates (Baumgartner et al., 2021), and a pronounced increase in Thioflavin fluorescence in cell homogenates (**Figure 2K**), both telltale markers of elevated proteotoxicity (Kandel et al., 2024)**.**

These findings indicate that *hsrω* loss disrupts ribosome integrity and proteome surveillance, fostering oxidative stress and proteotoxicity. The resulting translational stress therefore compromises cellular fitness, predisposing *hsrω*^{66} cells to elimination (**Figure 1I**) through competition with the neighboring wild type cells. Thus, the cell-competition phenotype of *hsrω*

mutants—and, by extension, the functional compromise of the omega speckle biomolecular condensate—culminates in impaired cellular proteostasis and compromised stress adaptation.

hsrω displays haploinsufficiency for tumor suppression

We next tested the survival of *lgl* somatic clones in *hsrω*^{66}/+ larvae, given that perturbed proteostasis permits tumor progression in other contexts, such as the *Minute* genetic background (Baumgartner et al., 2021; Khan et al., 2013). In a wild type epithelium, somatic clones lacking Lgl are recognized and eliminated by a tissue surveillance mechanism known as cell competition (Khan et al., 2013; Menéndez et al., 2010; Suijkerbuijk et al., 2016). These clones display increased cellular stress (**Figure S2**), exhibit elevated cell death, and are basally extruded ((Khan et al., 2013), also see **Figure 3A**). By contrast, *lgl* clones generated in *hsrω*^{66}/+ wing imaginal discs evaded elimination and underwent neoplastic transformation, marked by disrupted cortical F-Actin (**Figure 3B, C**). Consistent with the acquisition of a 'winner' cell state, we observed cell death in *lgl*$^{+}$/*lgl* cells along the *lgl* clone boundaries (**Figure 3B**). Furthermore, these transformed *lgl* clones displayed elevated cell proliferation (pH3, **Figure 3D**) and an increase in Matrix Metalloproteinase-1 (MMP1; **Figure 3E**), indicating ECM degradation and the acquisition of invasive properties (Beaucher et al., 2007). We thus hypothesized that the compromised proteostasis in the *hsrω* mutant background (**Figure 2**) would render the epithelium hypersensitive to proteosome inhibitor. Indeed, administration of the classical proteasome inhibitor MG-132 (Chen et al., 2011) compromised the tumor susceptibility of *hsrω*^{66}/+ larvae, reducing *lgl* tumor burden in a dose-dependent manner (**Figure 3F**). This suggests that the tumor-promoting environment of *hsrω* haploinsufficiency relies on a precarious proteostasis balance.

We next asked if this tumor susceptibility was driven by the loss of structural integrity of the omega speckle. A hallmark of condensate-based regulatory systems is their sensitivity to component dosage—both depletion and overexpression can perturb phase separation (Shin and Brangwynne, 2017) also recapitulated by omega speckles that are sensitive to doses of *hsrω* and omega speckles-associated hnRNPs such as Hrb87F (Lakhotia, 2011; Prasanth et al., 2000). Consistent with this model, we found that *lgl* somatic clones underwent neoplastic transformation not only upon *hsrω* knockdown (*UAS-hsrω-RNAi*; **Figure 3G-I**) but also upon overexpression (*UAS-hsrω*^{EP3037}; **Figure 3J, K**). Under both conditions, *lgl* clones gained a growth advantage, induced cell death in the neighboring cells (**Figure 3G**), and upregulated invasion markers (MMP1; **Figure 3I**).

To confirm that condensate integrity is the critical factor, we manipulated other structural components. Heterozygosity of *Df(3R)Hrb87F*—which encodes an hnRNP localized to omega speckles—similarly promoted *lgl* transformation (**Figure S3A**). Moreover, downregulating the chromatin remodeling ATPase *ISWI*—required for omega speckle structural integrity (Onorati et al., 2011; Singh and Lakhotia, 2015)—also facilitated neoplastic transformation (**Figure S3C**). Finally, *lgl* somatic clones induced in the adult intestinal epithelium of *hsrω*^{66}/+ adult flies also displayed neoplastic transformation (**Figure S4**), unlike those generated in a WT background. This indicates that *hsrω* haploinsufficiency creates a tumor-susceptible host

genetic background, likely through sensitivity to biocondensates disruption and ensuing impaired protein homeostasis.

Tumor inhibitory role of redox regulators Nrf2-Keap1 and inflammatory protein dSTING

To validate the versatility of haploinsufficiency screening in uncovering diverse host genetic determinants, we extended our analysis to two other functional classes of stress regulators identified in our screen: the redox sensor Nrf2-Keap1 and the viral immune sensor cGAS-STING. While somatic variations in these pathways are suspected to influence cancer risk (Michalak and Michalak, 2025) their direct impact on intrinsic tumor surveillance remains to be functionally dissected in a host genetic model.

First, we examined the Nrf2-Keap1 oxidative stress pathway. This conserved system mediates cellular responses to oxidative damage as Keap1 suppresses the transcription factor Nrf2 (*Drosophila* homolog, CncC) by targeting it for proteasomal degradation (Fuse and Kobayashi, 2017). In the absence of Keap1, CncC translocates to the nucleus to activate antioxidant and proteostasis genes (Radhakrishnan et al., 2010). We reasoned that altering this redox balance might shield emerging tumor cells from oxidative stress-induced elimination. Consistent with this, *lgl* somatic clones generated in a *Keap1* haploinsufficient background ($Keap1^{EY5}/+$) exhibited enhanced growth and neoplastic transformation (**Figure 4A**) when compared to *lgl* clones generated in wild type genetic background. We observed a similar tumor-promoting effect upon cell-autonomous downregulation of *Keap1* (*lgl; UAS-Keap1-RNAi*; **Figure 4B, C**) or direct genetic gain of *CncC* (*lgl; UAS-CncC*; **Figure 4D**), with transformed *lgl* clones displaying elevated cell death in abutting wild type neighbors (**Figure 4C**). This suggests that constitutive activation of antioxidant defense (via *Keap1* loss) acts as a barrier to the elimination of oncogenic clones.

Next, we investigated the cGAS–STING pathway. This pathway acts as a sentinel for aberrant cytosolic DNA—a hallmark of genomic instability and cellular damage or of virus-induced biotic stress (Hopfner and Hornung, 2020). In *Drosophila*, activation of dSTING triggers an inflammatory response via the NF-κB/Relish pathway (Cai et al., 2020; Martin et al., 2018). We hypothesized that haploinsufficiency of *dSTING* would impair the host's ability to sense and eliminate early oncogenic clones. Indeed, *lgl* somatic clones generated in a *dSTING* mutant background ($dSTING^{\Delta RG5}/+$) showed enhanced survival and underwent neoplastic transformation (**Figure 4E**), effectively phenocopying the $hsr\omega^{66}/+$ tissue. Similarly, cell-autonomous *dSTING* knockdown within *lgl*-deficient clones led to robust tumor formation (**Figure 4F**), confirming that innate immune sensing is required for effective tumor surveillance.

Finally, we explored the potential crosstalk between these mechanisms. While identified independently, our data suggests a functional link between nuclear condensates and immune surveillance. Notably, we observed that compared to wild type larval salivary glands, the $hsr\omega^{66}$ mutant cells displayed disrupted dSTING punctae with reduced diffuse distribution in

239 cytoplasm (**Figure 4G, H** and **Figure S5**). This suggests that the condensate defects in *hsrω*
240 mutants may compromise dSTING trafficking or assembly. This was confirmed by marked
241 suppression of *lgl* tumor growth following treatment with the dSTING agonist (**Figure 4I**) 2′3′-
242 cGAMP (Cai et al., 2020). This demonstrates that pharmacological reactivation of innate
243 immunity can compensate for the surveillance deficits caused by *hsrω* loss, highlighting a
244 functional intersection between nuclear condensates and immune signaling.

245

246 **CNVs in human homologs of stress regulators and Sat III correlate with cancer severity**

247 To evaluate the clinical relevance of our findings in *Drosophila*, we investigated whether
248 genetic alterations in the human homologs of these stress regulators correlate with patient
249 outcomes. First, we examined if variations in gene dosage affect the survival of cancer patients
250 using the Cancer Genome Atlas (TCGA). We analysed Copy Number Variations (CNVs) in
251 human *KEAP1* and *STING1* across diverse cancer types (**Figures S6A, B)**. Although TCGA
252 data primarily reflects somatic alterations of tumor origin, it provides a window into how gene
253 dosage impacts progression. Kaplan-Meier survival plots revealed a significant correlation
254 between CNVs in these genes (including deletions and amplifications) and poor patient
255 survival (**Figures S6A, B**). This confirms that, similar to our *Drosophila* models, the dosage of
256 these stress regulators is a critical determinant of human cancer prognosis.

257 Next, we focused on the human functional analog of *hsrω*, the *Satellite III* (*Sat III*) repeats.
258 While *hsrω* lacks a sequence homolog in mammals, the *Sat III* repeats at the pericentromeric
259 region of chromosome 9 (9q12) are its functional analog (Jolly and Lakhotia, 2006; Jolly et al.,
260 2004). Like *hsrω*, *Sat III* is actively transcribed during stress to form phase-separated nuclear
261 'stress bodies' (Jolly et al., 2004; Goenka et al., 2016). These bodies sequester Heat Shock
262 Factor 1 (HSF1) and specific RNA-binding proteins. Since repetitive *Sat III* sequences are not
263 resolved in standard TCGA exome data, we first looked at its obligate binding partner, HSF1.
264 Notably, TCGA analysis revealed that CNVs in HSF1 are also associated with poor patient
265 survival (**Figure 5A, B**), thereby supporting the importance of the stress body machinery.
266 Finally, we tested the hypothesis that germline variations in *Sat III* itself act as a host
267 susceptibility factor. Since *Sat III* resides in a large heterochromatic block of pentameric repeats
268 at 9q12 (**Figure 5C**), we utilized digital droplet PCR (ddPCR) to precisely quantify copy
269 number variations in *Sat III* using the 9q12-specific, pHuR98 probe (de Lima et al., 2021; Jolly
270 et al., 2002). We analysed genomic DNA from prostate cancer patients and compared them to
271 benign controls. Strikingly, we observed significant germline copy number variations in *Sat III*
272 in patients with high cancer severity (Gleason scores 6–10) compared to benign controls
273 (**Figure 5D**). Further, reminiscent of the tumor-promoting effects of *hsrω* haploinsufficiency
274 in flies, we also observed an overall decrease in Sat III transcript levels across different prostate
275 cancer cell lines compared to benign control (**Figure 5E**). This agrees with previous report that
276 *Sat III* is misregulated in cancer cell lines (Chatterjee and Sengupta, 2022).

277 Collectively, our findings in *Drosophila* and human cancers show that perturbations in the
278 dosage of stress surveillance components, whether the protein coding *KEAP1* and *STING1* or

the noncoding *hsrω*/*Sat III* architectural RNAs, are broadly associated with cancer susceptibility, severity and poor prognosis.

Discussion

Our study establishes *Drosophila* haploinsufficiency screen as a powerful tool for identifying host genetic regulators of cancer susceptibility **(Figure 6)**, a class of genes often overlooked by traditional oncogene/tumor suppressor screens. While the roles of high-penetrance mutations (e.g., TP53, PTEN) are well defined (Berger and Pandolfi, 2011), the genetic architecture of host resistance remains underexplored. We demonstrate that subtle genetic deficits (haploinsufficiency) in fundamental homeostatic regulators, specifically the nuclear condensates, redox sensors, and immune sentinels, do not initiate tumors per se, but severely erode the 'surveillance buffer' of cells. This renders the epithelium permissive to neoplastic transformation upon a second hit, such as loss of the cell polarity protein Lgl.

A major finding of this study is the identification of the lncRNA-encoding *hsrω*, essential for formation of omega speckle biomolecular condensates, as a key suppressor of susceptibility. This expands the "Proteostasis Addiction" model of cancer (Dai and Sampson, 2016). We propose that *hsrω*- dependent omega speckle condensates function as proteostasis regulator by, sequestering various RNA-binding proteins, and buffering the translational stress. Loss of this buffer, as in *hsrω* haploinsufficiency, creates a 'proteostasis-vulnerable' epithelium that cannot cope with the physiological demands of emerging oncogenic clones, which effectively lowers the threshold for tumorigenesis. This mirrors the classic Minute phenotype in *Drosophila* (Baumgartner et al., 2021), but with a crucial distinction that in this case a non-coding RNA rather than a ribosomal protein acts as the linchpin of surveillance.

Validating the breadth of our screening strategy, we independently identified *STING* (an innate immunity factor) and *Keap1* (a redox regulatory factor) as host modifiers. While distinct in function, these pathways likely converge. Our observations that *hsrω* loss disrupts the cellular distribution of dSTING, and that STING agonists can rescue the *hsrω* tumor susceptibility phenotype suggest a functional intersection. We postulate that the dynamics of omega speckle nuclear condensates also regulate the nucleocytoplasmic distribution or availability of specific immune or redox factors, such as STING. Thus, *hsrω*, *STING*, and *Keap1* may function as nodes in an integrated 'Stress Surveillance Network.' Disabling any node, whether by compromising activities of the hsrω or the sensors (STING/Keap1), collapses the network, which in turn permits cells carrying tumorigenic hits overcome tumor suppressive cell competition.

A significant implication of our study is the potential translational link to human *Sat III* repeats. Although the *Sat III* repeats have long been considered "junk DNA" or mere markers of stress, in context of the *Drosophila* model, we suggest a significant tumor-suppressive function to this non-coding locus. Our finding that the germline Copy Number Variations (CNVs) in *Sat III* correlate with prostate cancer severity suggests that the highly polymorphic repetitive regions of the human genome, often ignored in standard exome sequencing, may harbor critical determinants of cancer susceptibility. Just as *hsrω* dosage dictates fly cells' tumor resistance,

the intrinsic copy number of human *Sat III* may determine the robustness of a patient's "cellular stress response", thereby influencing clinical prognosis.

Finally, our findings resonate with the evolutionary concept that cancer resistance is a distinct trait from tumor suppression (Klein, 2009). Long-lived mammals, such as elephants or whales, have evolved redundant resistance mechanisms, including increased TP53 copy numbers (Sulak et al., 2016). We propose that *hsrω/Sat III*, STING, and Keap1 represent a similar layer of 'background' resistance. These genes do not drive the cancer, but they set the rules of engagement. A host with robust condensate dynamics and immune sensing (high resistance) forces oncogenes to overcome a steep barrier, whereas a host with haploinsufficient defects (low resistance) provides a more permissive environment. Combining *Drosophila* genetics with human CNV analysis opens a new avenue to systematically map these elusive 'host resistance' genes, moving the field beyond the tumor-centric driver model towards a more holistic understanding of cancer susceptibility.

Acknowledgement

We acknowledge Bloomington Drosophila Stock Centre (Indiana University) for fly stocks and Developmental Studies Hybridoma Bank (University of Iowa) for antibodies. Ethical approval for use of patient samples in this study was obtained from the Institutional Ethics Committee (IEC) at Indian Institute of Technology Kanpur (Approval Number: IITK/IEC/2020-21/II/05) issued on February 18, 2021 for five years. All patients participating in this study provided written informed consent. We thank S. Ganesh, Indian Institute of Technology Kanpur, for the gift of the FK2 anti-ubiquitin antibody. This work was supported by the Department of Biotechnology, Govt. of India and Wellcome Trust India Alliance (IA/E/13/1/501271) and Department of Science and Technology, DST/WOS-A/LS-75/2021 to AB. Support by the Science & Engineering Research Board (SERB), Department of Science and Technology, Govt. of India (CO/S5/AB-03/2017) to PS and DBT/ Wellcome Trust India Alliance (IA/S/19/2/504659) to BA is acknowledged. SCL is supported by the Department of Biotechnology, Ministry of Science and Technology (BT/PR32126/BRB/10/1775/2019) and the Science & Engineering Research Board, Govt. of India, as a Distinguished Fellow (SB/DF/009/2019).

The authors declare no competing interests.

Material and Methods

Fly Stocks

Fly stocks were maintained at 25° C on standard fly food containing corn powder, yeast, and sugar. The following mutant/transgenic lines were used in this study: *w; l(2)gl^{4} FRT40A/CyO* (#36289, BDSC); *w; w; hsrω^{66}/TM6B* (Johnson et al., 2011); *w;UAS-hsrω-RNAi(2x)*(Mallik and Lakhotia, 2009); *EP3037/ EP3037* (Mallik and Lakhotia, 2009); *Df(3R)Hrb87F/Tb* (#67701, BDSC); *y w hs-flp, tub-Gal4, UAS-GFP/; tub-Gal80 FRT40A/CyO; w; FRT82B* (#86313, BDSC); *y w hs-flp; FRT82B Ubi-GFP* (#5188, BDSC); *w; TRE-DsRed;+ (*#59011,

BDSC);*UAS-STING RNAi* (#31565, BDSC); *w;+;th-lacZ* (Bennett and Harvey, 2006); *STING*$^{\Delta RG5}$ (Martin et al., 2018); *Keap*^{EY5} (Gift from Dirk Bohmann (Sykiotis and Bohmann, 2008)). BDSC: Bloomington Drosophila Stock Center, Indiana University Bloomington.

Genotypes of clone and method clone induction:

Heat shock induced somatic clones were generated using the flp/FRT technique (Xu and Rubin, 1993) or MARCM technique (Lee and Luo, 1999). Heat shock was given at 37°C for 30 minutes to early second instar progeny larvae (48 hours after egg laying, ARL) of the following parental genotypes. The larvae were then grown at 25°C till 96 to 120 hours AEL.

- ***hsrω*^{66} mutant** clones **(**non-GFP) and its twin spot (two copies of GFP): *FRT82B hsrω*^{66}*/ TM3b* X *y w hs-flp; FRT82B Ubi-GFP*
- ***lgl*$^{-}$ clones in *hsrω*^{66}/+ genetic background:** *lgl*^{4} *FRT40A/Cy-O;hsrω*^{66}*/ TM3b* and *y w hs-flp tub Gal4 UAS-GFP; tub-Gal80 FRT40A/Cy-O*
- ***lgl*$^{-}$ clones in *Df(3R)Hrb87F)/*+ genetic background:** *lgl*^{4} *FRT40A/Cy-O;Df(3R)Hrb87F/TM3b* and *y w hs-flp tub Gal4 UAS-GFP; tub-Gal80 FRT40A/Cy-O*
- ***lgl*$^{-}$ *UAS-hsrω-RNAi*** and ***lgl*$^{-}$ *UAS-hsrω* ^{EP3037}**: *lgl*^{4}*UAS-hsrω RNAi (2X) FRT40A;* and *y w hs-flp tub Gal4 UAS-GFP; tub-Gal80 FRT40A/Cy-O.* or *lgl*^{4}*FRT40A; hsrω*^{EP3037} and *y w hs-flp tub Gal4 UAS-GFP; tub-Gal80 FRT40A/Cy-O* respectively.
- ***lgl*$^{-}$ in *STING*$^{\Delta 5}$/+ genetic background:** *lgl*^{4} *FRT40A, STING*$^{\Delta 5}$*/Cy-O* and *y w hs-flp tub Gal4 UAS-GFP; tub-Gal80 FRT40A/Cy-O*
- ***lgl*$^{-}$ *UAS-STING-RNAi:*** *w;lgl*^{4} *FRT40A UAS-STING RNAi/Cy-O;+* and *y w hs-flp tub Gal4 UAS-GFP; tub-Gal80 FRT40A/Cy-O*
- ***lgl*$^{-}$ in *Keap1*^{EY5}/+ genetic background:** *w;lgl*^{4} *FRT40A Keap1*^{EY5}*/Cy-O;+* and *y w hs-flp tub Gal4 UAS-GFP; tub-Gal80 FRT40A/Cy-O*
- ***lgl*$^{-}$ *UAS-STING-RNAi:*** *w;lgl*^{4} *FRT40A UAS-keap1RNAi/Cy-O;+* and *y w hs-flp tub Gal4 UAS-GFP; tub-Gal80 FRT40A/Cy-O*
- ***lgl*$^{-}$ *UAS-CncC:*** *w;lgl*^{4} *FRT40A UAS-CncC/Cy-O;+* and *y w hs-flp tub Gal4 UAS-GFP; tub-Gal80 FRT40A/Cy-O*

Immunofluorescence staining and microscopy

Larvae of desired genotypes were dissected in 1x Phosphate Buffer Saline (PBS), and imaginal discs were fixed in 4% paraformaldehyde in 1x PBS containing 0.02 % Triton-X-100, and incubated overnight in the desired primary antibody at 4^{0}C, followed by washing and incubation with appropriate fluorescently tagged secondary antibodies for two hours at the room, and counterstained with SYTOX-Green (S33025, Invitrogen) or Alexa Fluor™ 633 Phalloidin (A22284, Invitrogen). The following primary antibodies were used: anti-Caspase-3, rabbit (1:500 dilution, MERK/Sigma Aldrich, C8487), Polyubiquitinylated conjugates monoclonal antibody FK1, mouse (1:500 dilution, Enzo Life Sciences, BML-PW8805-0500), Anti-phospho Histone-3 (pSer^{10}), rabbit (1:500 dilution, MERK /Sigma Aldrich H0412), anti- β Galactosidase, mouse (1:200 dilution, MERK/Sigma Aldrich, G6282). To detect MMP1, we used a cocktail of

monoclonal antibodies raised in mice (3A6B4, 3B8D12, 5H7B11, and 3B8D12; 1:1:1:1 ratio at a final dilution of 1:300, Developmental Studies Hybridoma Bank (DSHB), University of Iowa), anti-Fasciclin III, Fas III, mouse, (7G10, DSHB). Anti-dSTING, rabbit (1:100, (Martin et al., 2018)). We used the following secondary antibodies from Invitrogen: Alexa Fluor™ 555 anti-mouse (A32727) and Alexa Fluor 555 anti-rabbit (A32732).

Nuclear staining was carried out using either SYTOX-Green (Invitrogen #S33025) at 1:300 or To-PRO (Invitrogen, #T3605) at 1:1000 dilution. Corticular F-Actin was labeled using Alexa Fluor™ 633 Phalloidin (#A22284, Invitrogen). After washing, the discs were mounted using a Vectashield anti-fade medium (Vector Laboratories, H-1000). Images were acquired with a Leica-SP5 confocal microscope and processed using the Leica confocal software LAS AF. Images were acquired using a 20x or a 40x (oil immersion) objective. Images of GFP-marked *lgl*; *hsrω*^{66}/+ tumor-bearing larvae were acquired with a Leica M205FA stereomicroscope with epi-fluorescent illumination (excitation filter 480 nm). All images were assembled using Adobe Photoshop CS5 software.

For detecting protein aggregates, the wing imaginal discs were dissected out from larvae of the desired genotype and age in PBS and fixed in 4% formaldehyde in 1× PBS, followed by permeabilization in 0.4% Triton X-100 and 3mM ethylenediaminetetraacetic acid (pH 8.0) in 1× PBS. Fixed imaginal discs were subsequently incubated in ProteoStat detection reagent (1:10,000 dilution, Enzo Life Sciences, #ENZ-51023-KP050), washed in 1XPBS, and the wing imaginal discs were mounted in glycerol-based anti-fade and imaged using Leica-SP5 confocal microscope. We used LysoTracker® Red DND-99 dye (#L7528, Thermo-Fisher Scientific/Invitrogen) to detect acidic lysosomes and MitoTracker™ Red CMXRos (#M22425, Thermo-Fisher Scientific/Invitrogen). This cell-permeant, red-fluorescent dye stains mitochondria in live cells and is a marker for altered membrane potential. Briefly, larvae of the desired genotype were gently rinsed and dissected in 1x PBS to remove tissues like fat body, gut, etc. The flipped larvae were incubated in freshly prepared 500nM of LysoTracker (in 1X PBS) or 500nM MitoTracker (in 1X PBS) at room temperature in the dark for 15 minutes, followed by a thorough rinse in 1x PBS. Unfixed wing discs were mounted in anti-fade-containing Vectashield (Vector Laboratories, #H-1000), and images were acquired immediately using a Leica-SP5 confocal microscope and processed using Leica confocal software-LAS AF and assembled using Adobe Photoshop.

We used dihydroethidium (#D11347, Invitrogen), a free radical sensitive dye, to detect ROS levels in unfixed larval tissues (Owusu-Ansah et al., 2008). Briefly, larvae of the desired genotype were washed and dissected in 1xPBS. After removing the fat body, gut, and other adherent tissues, the flipped larvae were incubated in freshly made 1:1000 DHE at room temperature in the dark for 15 minutes. The wing imaginal discs were subsequently thoroughly rinsed in 1XPBS, mounted in anti-fade containing Vectashield (Vector Laboratories, #H-1000), and images were acquired with Leica-SP5 confocal microscope and processed using Leica confocal software-LAS AF and AdobePhotoshop CS3.

Clone size and Fluorescence Quantification

ImageJ platform ((Schneider et al., 2012) , http://rsb.info.nih.gov/ij/) was used for image analysis. For measuring size of wing discs, confocal projection images acquired with a

445 Leica-SP5 confocal microscope were projected as a single image and used as the input file.
446 The Freehand selection tool was used to trace the outline of the imaginal discs marked by
447 nuclear fluorescence, and the "Measure" option was used to obtain the area of the wing disc in
448 arbitrary units. For clone size quantification freehand selection tool was used to trace the
449 outline of the nuclear GFP-marked clones in individual discs. For quantification of $hsr\omega^{66}$
450 mutant clones (marked by complete loss of GFP) and their twin spots (hsr^{+} *GFP/* hsr^{+}*GFP*)
451 characterized by their brighter GFP fluorescent was calculated using "Analyze Particle" option
452 of Image J platform on confocal projection images. Images were first converted to an 8-bit
453 format; signal thresholds were set to calculate the number of pixels with no signal (non-
454 GFP, $hsr\omega^{66}/hsr\omega^{66}$ clones) and those with double GFP (twin spots, +/+). To quantify total
455 fluorescence (for pH3/DHE/TRE-dsRED/γH2AX/Lysotracker/ProteoStat) confocal
456 projection images of the red channel of individual wing imaginal discs was used as input
457 file after converting to 8-bit formats. Image J was used to overlay a grid of uniform unit size,
458 and the maximum fluorescence intensity per ROI was recorded. Graphs were plotted using MS
459 Excel.

460 **ThT Assay for estimating protein aggregates**

461 Larval wing discs were homogenized in ice cold 1xPBS to release cellular contents, including
462 any insoluble amyloid-like aggregates. Thioflavin T (ThT) at a final concentration of 10μM
463 was added to the homogenate and incubate for 10 minutes at room temperature. ThT
464 selectively binds to β-sheet-rich protein aggregates, such as amyloids, leading to a significant
465 increase in its fluorescence. The homogenate was transferred to a black 96-well plate and
466 fluorescence was measured at excitation of 440–450 nm and emission at 480–490 nm using
467 a plate reader (Bio-Rad).

468 **Proteomics of wing imaginal discs from $hsr\omega^{66}$ mutant and $Canton^{S}$ larvae**

469 - **Protein extraction from wing discs of third instar larvae**

470 Wing imaginal discs from third instar larvae were dissected in cold 1× PBS put in 100 µl
471 extraction buffer (6 M GnHCl in 50 mM Tris-HCl pH 7.4, 65 mM dithiothreitol) with 50 mM
472 sodium acetate and protease inhibitors (1× protease inhibitor cocktail with 0.2 mM PMSF).
473 Within 30 minutes of dissection the wing discs were sonicated with a Bioruptor (Diagenode)
474 using 30 s ON and 30 s OFF for 5 cycles at 4°C. Cell debris was removed by centrifuging at
475 6000 g for 3 minutes and supernatant transferred to a new tube. The protein concentration
476 was determined spectrophotometrically using Nanodrop. Five micrograms of the protein were
477 used for LC-MS-MS analysis.

478 - **Sample preparation for LC-MS/MS**

479 Five micrograms of the protein samples were reduced with 5 mM tris(2-carboxyethyl)
480 phosphine (TCEP), further alkylated with 50 mM iodoacetamide and digested with Trypsin
481 (1:50, Trypsin/lysate ratio) for 16 h at 37°C. Digests were cleaned using a C18 silica cartridge
482 to remove the Digests were cleaned using a C18 silica cartridge to remove the salt and dried
483 using a speed vac. The dried pellet was resuspended in buffer A (2% acetonitrile, 0.1% formic
484 acid).

485 • **Mass Spectrometric Analysis of Peptide Mixtures**
486
487 Experiments were performed on an Easy-nlc-1000 system coupled with an Orbitrap Exploris
488 mass spectrometer. 1ug of peptide sample were loaded on C18 column 15 cm, 3.0µm Acclaim
489 PepMap (Thermo Fisher Scientific) and separated with a 0–40% gradient of buffer B (80%
490 acetonitrile, 0.1% formic acid*)* at a flow rate of 300 nl/min) and injected for MS analysis. LC
491 gradients were run for 60 minutes. MS1 spectra were acquired in the Orbitrap (Max IT = 25ms,
492 AGQ target = 300%; RF Lens = 70%; R=60K, mass range = 375−1500; Profile data). Dynamic
493 exclusion was employed for 30s excluding all charge states for a given precursor. MS2 spectra
494 were collected for top 12 peptides. MS2 (Max IT= 22ms, R= 15K, AGC target 200%).
495
496 • **Data Processing**
497
498 All samples were processed and RAW files generated were analyzed with Proteome Discoverer
499 (v2.5) against the Uniprot Drosophila melanogaster database. For dual Sequest and Amanda
500 search, the precursor and fragment mass tolerances were set at 10 ppm and 0.02 Da,
501 respectively. The protease used to generate peptides, i.e., enzyme specificity was set for
502 trypsin/P (cleavage at the C terminus of "K/R: unless followed by "P"). Carbamidomethyl on
503 cysteine as fixed modification and oxidation of methionine and N-terminal acetylation were
504 considered as variable modifications for database search. Both peptide spectrum match and
505 protein false discovery rate were set to 0.01 FDR.

506 • **Proteome data analysis**

507 To identify biologically relevant protein signatures in *hsrω*^{66} wing disc proteome versus wild
508 type proteome we calculated the log2 abundance ratios, using mean abundance values for
509 individual UniProt IDs. Only those with combined FDR confidence <0.05 (medium) or <0.01
510 (high) were taken into consideration; those with combined FDR >0.05 (low) were discarded.
511 We further filtered out peptides that were not detected in either MS or MS/MS spectra
512 depending on the peak calling. Overall 3125 Uniprot IDs were subjected to function
513 enrichment analysis using STRING platform (https://string-db.org/, (Szklarczyk et al.,
514 2021)) in conjunction with ssGSEA (single-sample Gene Set Enrichment Analysis).

515 **Kaplan-Meier survival plots**

516 Kaplan-Meier survival plots were generated using clinical data from TCGA (The cancer
517 genome atlas), using cBioPortal platform (https://www.cbioportal.org/). Datasets were
518 restricted to epithelial cancers only and queried for CNA (Copy Number Alterations) and
519 mutations for individual genes: *KEAP1*, *HSF1* and *STING1*.

520 **Study of *Sat III* germline copy number variations in PCa patients**

521 • **Study population and patient recruitment**

522 The peripheral blood used in this study was collected from the biopsy-confirmed treatment-
523 naïve prostate cancer (PCa) patients (n=18) and benign prostatic hyperplasia (BPH) patients
524 (n=5), enrolled at the Department of Urology, King George's Medical University (KGMU,

525 Lucknow, India). Clinical specimens were collected after obtaining written informed consent
526 and institutional review board approvals from KGMU and Indian Institute of Technology
527 Kanpur (Kanpur, India). The study was initiated after obtaining approval from the
528 Institutional Ethics Committee.

529 **Digital droplet PCR quantification of SatIII copy number in PCa patients**

530 Blood was collected in K_2-EDTA 2ml tubes from BPH (benign prostatic hyperplasia) and
531 PCa (prostate cancer) patients. Genomic DNA was isolated using QIAamp® DNA Blood
532 mini-kit (#51104, Qiagen), which was further processed to identify *Sat III* copies. Droplet
533 digital PCR was performed with the QX200 Droplet Digital PCR System (#1864001,Bio-
534 Rad, USA). The ddPCR reaction mixture consisted of 10µL of 2XddPCR Supermix for
535 Probes (#1863026, Bio-Rad, USA), 10pg of genomic DNA, and 20Xprimers/probes mix in a
536 final volume of 20µL. The entire reaction mixture was loaded into a sample well of a DG8
537 Cartridge (Bio-Rad, USA) together with 70µL of droplet generation oil (Bio-Rad, USA) and
538 placed into the automated droplet generator (Bio-Rad, USA). After processing, the droplets
539 generated from each sample were transferred to a 96-well PCR plate (Bio-Rad,USA). PCR
540 amplification was carried out on a T100 Touch thermal cycler (Bio-Rad, USA) using a
541 thermal profile beginning at 95 °C for 10 min, followed by 40 cycles of 94 °C for 30 s, and
542 60 °C for 60 s, and ending of 98 °C for 10 min at a ramp rate of 2 °C/s. After PCR, the plate
543 was loaded on the droplet reader (Bio-Rad, USA); acquired data were analyzed with
544 QuantaSoft Analysis Pro software (Bio-Rad, USA). All samples had ≥10000 accepted
545 droplets to be considered for analysis. SatIII copies were determined by QuantaSoft, the
546 software coupled to the Droplet Reader QX200 that applies a Poisson algorithm to calculate
547 the initial concentration of DNA target molecules as units of copies/µL input based on
548 positive and negative droplets. Specifically, after setting an appropriate fluorescence
549 threshold to determine the number of positive droplets (containing at least one target
550 molecule), the software calculates the number of copies per µL of the reaction volume.

551 Student's *t*-test was applied to determine the statistical significance for independent samples
552 p-value. Violin plots show the median and quartiles.

553 **Sat III expression analysis in cancer cell lines**

554 - **Cancer cell lines and culture conditions**

555 22RV1, PC3, VCaP, LNCaP (Prostate cancer cell lines), were obtained from American Type
556 Culture Collection (ATCC) and were cultured as per the ATCC recommended guidelines.
557 Briefly, the cells were cultured in a growth medium supplemented with 10% fetal bovine serum
558 (FBS) and 0.5% Penicillin-Streptomycin (Gibco, Thermo-Fisher Scientific) in a cell culture
559 incubator (Thermo Fisher Scientific) supplied with 5% CO_2 at 37°C.

560 - **RNA isolation and Quantitative PCR (qPCR)**

561 The total RNA was extracted using RNAiso Plus (Takara), and 1µg of total RNA was reverse
562 transcribed into cDNA using First Strand cDNA synthesis kit (PureGene) according to the
563 manufacturer's protocol. Quantitative PCR (qPCR) was performed using cDNA template,

primer sets (sat III_FP: TATGAATTCAATCAACCCGAGTGCAATCGAA, sat III_RP: TATGGATCCTTCCATTCCATTCCTGTACTCG; GAPDH_FP: TGCACCACCAACTGCTTAGC, GAPDH_RP: GGCATGGACTGTGGTCATGAG) and SYBR Green PCR Master-Mix (PureGene) on the QuantStudio 5 Real-Time PCR System (Applied Biosystems). Relative sat III expression was calculated for each sample by the $\Delta\Delta C_T$ method. A two-tailed unpaired Student's t-test was applied to determine the statistical significance for independent samples $*P \leq 0.05$ and $**P \leq 0.001$. Error bars represent mean ± SEM.

References

Agrawal, N., Kango, M., Mishra, A. and Sinha, P. (1995). Neoplastic transformation and aberrant cell-cell interactions in genetic mosaics of lethal(2)giant larvae (lgl), a tumor suppressor gene of Drosophila. *Dev Biol* **172**, 218–229.

Aloke, C., Onisuru, O. O. and Achilonu, I. (2024). Glutathione S-transferase: A versatile and dynamic enzyme. *Biochem Biophys Res Commun* **734**, 150774.

Banani, S. F., Lee, H. O., Hyman, A. A. and Rosen, M. K. (2017). Biomolecular condensates: organizers of cellular biochemistry. *Nat Rev Mol Cell Biol* **18**, 285–298.

Baumgartner, M. E., Dinan, M. P., Langton, P. F., Kucinski, I. and Piddini, E. (2021). Proteotoxic stress is a driver of the loser status and cell competition. *Nat Cell Biol* **23**, 136–146.

Beaucher, M., Hersperger, E., Page-McCaw, A. and Shearn, A. (2007). Metastatic ability of *Drosophila* tumors depends on MMP activity. *Developmental Biology* **303**, 625–634.

Behrouzfar, K., Burton, K., Mutsaers, S. E., Morahan, G., Lake, R. A. and Fisher, S. A. (2021). How to Better Understand the Influence of Host Genetics on Developing an Effective Immune Response to Thoracic Cancers. *Front. Oncol.* **11**,.

Bendena, W. G., Garbe, J. C., Traverse, K. L., Lakhotia, S. C. and Pardue, M. L. (1989). Multiple inducers of the Drosophila heat shock locus 93D (hsr omega): inducer-specific patterns of the three transcripts. *J Cell Biol* **108**, 2017–2028.

Bennett, F. C. and Harvey, K. F. (2006). Fat Cadherin Modulates Organ Size in Drosophila via the Salvador/Warts/Hippo Signaling Pathway. *Current Biology* **16**, 2101–2110.

Berger, A. H. and Pandolfi, P. P. (2011). Haplo-insufficiency: a driving force in cancer. *J Pathol* **223**, 137–146.

Boija, A., Klein, I. A. and Young, R. A. (2021). Biomolecular Condensates and Cancer. *Cancer Cell* **39**, 174–192.

Cai, H., Holleufer, A., Simonsen, B., Schneider, J., Lemoine, A., Gad, H. H., Huang, J., Huang, J., Chen, D., Peng, T., et al. (2020). 2’3’-cGAMP triggers a STING- and NF-κB-dependent broad antiviral response in Drosophila. *Sci Signal* **13**, eabc4537.

Castro-Giner, F., Ratcliffe, P. and Tomlinson, I. (2015). The mini-driver model of polygenic cancer evolution. *Nat Rev Cancer* **15**, 680–685.

Chatterjee, M. and Sengupta, S. (2022). Human satellite III long noncoding RNA imparts survival benefits to cancer cells. *Cell Biol Int* **46**, 611–627.

603 **Chen, S., Wei, H.-M., Lv, W.-W., Wang, D.-L. and Sun, F.-L.** (2011). E2 Ligase dRad6 Regulates
604 DMP53 Turnover in Drosophila. *J Biol Chem* **286**, 9020–9030.

605 **Chenevix-Trench, G., Milne, R. L., Antoniou, A. C., Couch, F. J., Easton, D. F., Goldgar, D. E.,**
606 **and CIMBA** (2007). An international initiative to identify genetic modifiers of cancer risk in
607 BRCA1 and BRCA2 mutation carriers: the Consortium of Investigators of Modifiers of
608 BRCA1 and BRCA2 (CIMBA). *Breast Cancer Res* **9**, 104.

609 **Dai, C. and Sampson, S. B.** (2016). HSF1: Guardian of Proteostasis in Cancer. *Trends Cell Biol* **26**,
610 17–28.

611 **Datta, I., Vassel, T., Linkous, B., Odum, T., Drew, C., Taylor, A. and Bangi, E.** (2023). A targeted
612 genetic modifier screen in Drosophila uncovers vulnerabilities in a genetically complex model
613 of colon cancer. *G3 (Bethesda)* **13**, jkad053.

614 **de la Cova, C., Abril, M., Bellosta, P., Gallant, P. and Johnston, L. A.** (2004). Drosophila myc
615 regulates organ size by inducing cell competition. *Cell* **117**, 107–116.

616 **Froldi, F., Ziosi, M., Garoia, F., Pession, A., Grzeschik, N. A., Bellosta, P., Strand, D.,**
617 **Richardson, H. E., Pession, A. and Grifoni, D.** (2010). The lethal giant larvae tumour
618 suppressor mutation requires dMyc oncoprotein to promote clonal malignancy. *BMC Biol* **8**,
619 33.

620 **Fuse, Y. and Kobayashi, M.** (2017). Conservation of the Keap1-Nrf2 System: An Evolutionary
621 Journey through Stressful Space and Time. *Molecules* **22**, 436.

622 **Goenka, A., Sengupta, S., Pandey, R., Parihar, R., Mohanta, G. C., Mukerji, M. and Ganesh, S.**
623 (2016). Human satellite-III non-coding RNAs modulate heat-shock-induced transcriptional
624 repression. *J Cell Sci* **129**, 3541–3552.

625 **Hopfner, K.-P. and Hornung, V.** (2020). Molecular mechanisms and cellular functions of cGAS–
626 STING signalling. *Nat Rev Mol Cell Biol* **21**, 501–521.

627 **Johnson, T. K., Carrington, L. B., Hallas, R. J. and McKechnie, S. W.** (2009). Protein synthesis
628 rates in Drosophila associate with levels of the hsr-omega nuclear transcript. *Cell Stress*
629 *Chaperones* **14**, 569–577.

630 **Johnson, T. K., Cockerell, F. E. and McKechnie, S. W.** (2011). Transcripts from the Drosophila
631 heat-shock gene hsr-omega influence rates of protein synthesis but hardly affect resistance to
632 heat knockdown. *Mol Genet Genomics* **285**, 313–323.

633 **Jolly, C. and Lakhotia, S. C.** (2006). Human sat III and Drosophila hsr omega transcripts: a common
634 paradigm for regulation of nuclear RNA processing in stressed cells. *Nucleic Acids Res* **34**,
635 5508–5514.

636 **Jolly, C., Konecny, L., Grady, D. L., Kutskova, Y. A., Cotto, J. J., Morimoto, R. I. and Vourc'h,**
637 **C.** (2002). In vivo binding of active heat shock transcription factor 1 to human chromosome 9
638 heterochromatin during stress. *J Cell Biol* **156**, 775–781.

639 **Jolly, C., Metz, A., Govin, J., Vigneron, M., Turner, B. M., Khochbin, S. and Vourc'h, C.** (2004).
640 Stress-induced transcription of satellite III repeats. *J Cell Biol* **164**, 25–33.

641 **Kandel, R., Jung, J. and Neal, S.** (2024). Proteotoxic stress and the ubiquitin proteasome system.
642 *Seminars in Cell & Developmental Biology* **156**, 107–120.

Khan, S. J., Bajpai, A., Alam, M. A., Gupta, R. P., Harsh, S., Pandey, R. K., Goel-Bhattacharya, S., Nigam, A., Mishra, A. and Sinha, P. (2013). Epithelial neoplasia in Drosophila entails switch to primitive cell states. *Proc Natl Acad Sci U S A* **110**, E2163-2172.

Klein, G. (2009). Toward a genetics of cancer resistance. *Proc Natl Acad Sci U S A* **106**, 859–863.

Kongsuwan, K., Yu, Q., Vincent, A., Frisardi, M. C., Rosbash, M., Lengyel, J. A. and Merriam, J. (1985). A Drosophila Minute gene encodes a ribosomal protein. *Nature* **317**, 555–558.

Lakhotia, S. C. (2011). Forty years of the 93D puff of Drosophila melanogaster. *J Biosci* **36**, 399–423.

Lee, T. and Luo, L. (1999). Mosaic analysis with a repressible cell marker for studies of gene function in neuronal morphogenesis. *Neuron* **22**, 451–461.

Mah, L.-J., El-Osta, A. and Karagiannis, T. C. (2010). γH2AX: a sensitive molecular marker of DNA damage and repair. *Leukemia* **24**, 679–686.

Mallik, M. and Lakhotia, S. C. (2009). The developmentally active and stress-inducible noncoding hsromega gene is a novel regulator of apoptosis in Drosophila. *Genetics* **183**, 831–852.

Martin, M., Hiroyasu, A., Guzman, R. M., Roberts, S. A. and Goodman, A. G. (2018). Analysis of Drosophila STING Reveals an Evolutionarily Conserved Antimicrobial Function. *Cell Rep* **23**, 3537-3550.e6.

Martínez-Férriz, A., Ferrando, A., Fathinajafabadi, A. and Farràs, R. (2022). Ubiquitin-mediated mechanisms of translational control. *Semin Cell Dev Biol* **132**, 146–154.

Mehta, S. and Zhang, J. (2022). Liquid–liquid phase separation drives cellular function and dysfunction in cancer. *Nat Rev Cancer* **22**, 239–252.

Menéndez, J., Pérez-Garijo, A., Calleja, M. and Morata, G. (2010). A tumor-suppressing mechanism in Drosophila involving cell competition and the Hippo pathway. *Proc Natl Acad Sci U S A* **107**, 14651–14656.

Michalak, K. P. and Michalak, A. Z. (2025). Understanding chronic inflammation: couplings between cytokines, ROS, NO, Cai 2+, HIF-1α, Nrf2 and autophagy. *Front Immunol* **16**, 1558263.

Morata, G. and Ripoll, P. (1975). Minutes: Mutants of Drosophila autonomously affecting cell division rate. *Developmental Biology* **42**, 211–221.

Moreno, E., Basler, K. and Morata, G. (2002). Cells compete for decapentaplegic survival factor to prevent apoptosis in Drosophila wing development. *Nature* **416**, 755–759.

Onorati, M. C., Lazzaro, S., Mallik, M., Ingrassia, A. M. R., Carreca, A. P., Singh, A. K., Chaturvedi, D. P., Lakhotia, S. C. and Corona, D. F. V. (2011). The ISWI chromatin remodeler organizes the hsrω ncRNA-containing omega speckle nuclear compartments. *PLoS Genet* **7**, e1002096.

Owusu-Ansah, E., Yavari, A., Mandal, S. and Banerjee, U. (2008). Distinct mitochondrial retrograde signals control the G1-S cell cycle checkpoint. *Nat Genet* **40**, 356–361.

Prasanth, K. V., Rajendra, T. K., Lal, A. K. and Lakhotia, S. C. (2000). Omega speckles - a novel class of nuclear speckles containing hnRNPs associated with noncoding hsr-omega RNA in Drosophila. *J Cell Sci* **113 Pt 19**, 3485–3497.

Radhakrishnan, S. K., Lee, C. S., Young, P., Beskow, A., Chan, J. Y. and Deshaies, R. J. (2010). Transcription factor Nrf1 mediates the proteasome recovery pathway after proteasome inhibition in mammalian cells. *Mol Cell* **38**, 17–28.

Raetz, A. G. and David, S. S. (2019). When you're strange: Unusual features of the MUTYH glycosylase and implications in cancer. *DNA Repair (Amst)* **80**, 16–25.

Sabari, B. R., Dall'Agnese, A., Boija, A., Klein, I. A., Coffey, E. L., Shrinivas, K., Abraham, B. J., Hannett, N. M., Zamudio, A. V., Manteiga, J. C., et al. (2018). Coactivator condensation at super-enhancers links phase separation and gene control. *Science* **361**, eaar3958.

Sahu, R. K., Mutt, E. and Lakhotia, S. C. (2020). Conservation of gene architecture and domains amidst sequence divergence in the hsrω lncRNA gene across the Drosophila genus: an in silico analysis. *J Genet* **99**, 64.

Schneider, C. A., Rasband, W. S. and Eliceiri, K. W. (2012). NIH Image to ImageJ: 25 years of image analysis. *Nat Methods* **9**, 671–675.

Schulz, L., Ramirez, P., Lemieux, A., Gonzalez, E., Thomson, T. and Frost, B. (2023). Tau-induced elevation of the activity-regulated cytoskeleton associated protein Arc1 causally mediates neurodegeneration in the adult Drosophila brain. *Neuroscience* **518**, 101–111.

Settembre, C., Fraldi, A., Medina, D. L. and Ballabio, A. (2013). Signals from the lysosome: a control centre for cellular clearance and energy metabolism. *Nat Rev Mol Cell Biol* **14**, 283–296.

Shin, Y. and Brangwynne, C. P. (2017). Liquid phase condensation in cell physiology and disease. *Science* **357**, eaaf4382.

Singh, A. K. and Lakhotia, S. C. (2015). Dynamics of hnRNPs and omega speckles in normal and heat shocked live cell nuclei of Drosophila melanogaster. *Chromosoma* **124**, 367–383.

Siragusa, G., Tomasello, L., Giordano, C. and Pizzolanti, G. (2024). Survivin (BIRC5): Implications in cancer therapy. *Life Sci* **350**, 122788.

Suijkerbuijk, S. J. E., Kolahgar, G., Kucinski, I. and Piddini, E. (2016). Cell Competition Drives the Growth of Intestinal Adenomas in Drosophila. *Curr Biol* **26**, 428–438.

Sulak, M., Fong, L., Mika, K., Chigurupati, S., Yon, L., Mongan, N. P., Emes, R. D. and Lynch, V. J. (2016). TP53 copy number expansion is associated with the evolution of increased body size and an enhanced DNA damage response in elephants. *eLife* **5**, e11994.

Sykiotis, G. P. and Bohmann, D. (2008). Keap1/Nrf2 signaling regulates oxidative stress tolerance and lifespan in Drosophila. *Dev Cell* **14**, 76–85.

Szklarczyk, D., Gable, A. L., Nastou, K. C., Lyon, D., Kirsch, R., Pyysalo, S., Doncheva, N. T., Legeay, M., Fang, T., Bork, P., et al. (2021). The STRING database in 2021: customizable protein-protein networks, and functional characterization of user-uploaded gene/measurement sets. *Nucleic Acids Res* **49**, D605–D612.

Toba, G. and Aigaki, T. (2000). Disruption of the *Microsomal glutathione S-transferase-like* gene reduces life span of *Drosophila melanogaster*. *Gene* **253**, 179–187.

Turnbull, C., Sud, A. and Houlston, R. S. (2018). Cancer genetics, precision prevention and a call to action. *Nat Genet* **50**, 1212–1218.

Xu, T. and Rubin, G. M. (1993). Analysis of genetic mosaics in developing and adult Drosophila tissues. *Development* **117**, 1223–1237.

Zeng, H., Castillo-Cabrera, J., Manser, M., Lu, B., Yang, Z., Strande, V., Begue, D., Zamponi, R., Qiu, S., Sigoillot, F., et al. (2019). Genome-wide CRISPR screening reveals genetic modifiers of mutant EGFR dependence in human NSCLC. *Elife* **8**, e50223.

Zhang, Y., Lou, J., Liu, Y., Jin, P., Tan, Y., Song, H., Jin, W., Wang, D., Dong, F., Wu, S., et al. (2024). Phase separation of PML/RARα and BRD4 coassembled microspeckles governs transcriptional dysregulation in acute promyelocytic leukemia. *Proceedings of the National Academy of Sciences* **121**, e2406519121.

Figure Legends

Figure 1. *hsrω* mutant imaginal epithelia display cell stress and undergrowth

(**A**) Diagrammatic depiction of *hsrω* gene and its multiple nuclear and cytoplasmic transcripts (Sahu et al., 2020). The larger nuclear transcripts (RB, RG and RF) carry a long stretch of tandem repeats, providing a physical scaffold for binding hnRNPs, such as Hrb87F (Prasanth et al., 2000).

(**B**) Nuclear omega speckle biocondensates, marked by GFP-tagged Hrb87F (green) in wing imaginal disc cells. Nucleus is marked by To-PRO (blue).

(**C–F**) Third instar wing imaginal discs of $hsr\omega^{66}$/+ (C) and $hsr\omega^{66}$ (D) larvae immunostained for phospho-Histone 3 (pH3, red) to mark dividing cells, and quantification for wing disc size (E) and relative abundance of pH3-positive nuclei per arbitrary unit area (F).

(**G–I**) Expression of Caspase-3 (red) in $hsr\omega^{66}$/+ (G) and $hsr\omega^{66}$ (H) wing discs and quantification of Caspase-3 (fluorescence per ROI, I)

(**J-K**) Mosaic wing disc with $hsr\omega^{66}$ somatic clones (non-GFP) and their $hsr\omega^{66}$/+ twins (bright green, due to two copies of GFP). Boxed area in J is shown at a higher magnification to reveal Caspase-3 expression (red) in $hsr\omega^{66}$ cells abutting the clone's border. Comparison of $hsr\omega^{66}$clone areas with the twin-spot regions (K).

Scale bars 100µm in all confocal images, except in B' which is 10 µm.

Figure 2. $hsr\omega^{66}$ epithelium reveals cellular and proteotoxic stress

759 (**A**) Clustered heatmap displaying status of proteins significantly altered (±>$\log_2$
760 2-fold, $p < 0.05$, $q<0.05$) in *hsrω*^{66} versus wild type wing imaginal disc proteome. On the
761 right is the list of proteins upregulated (red) or downregulated (blue) in the *hsrω*^{66} proteome.

762 (**B**) Relative abundance ($\log_2$ fold change) of select ribosomal structural proteins in *hsrω*^{66}
763 proteome compared to its wild type counterpart.

764 (**C-D**) Rank-based Gene Ontology (GO) enrichment analysis of cytosolic and mitochondrial
765 ribosome proteins (C) and translation machinery (D). The x-axis represents the list of proteins
766 in ascending order of fold change in *hsrω*^{66} versus wild type. Black bars along the x-axis
767 mark the position of proteins being queried. The tables alongside give the protein levels of
768 the top five mis-expressed proteins belonging to a given GO class.

769 (**E**) Relative abundance of key DNA damage-associated proteins in *hsrω*^{66} proteome.

770 (**F-H**) Representative examples of wing imaginal discs displaying signatures of cellular
771 stress: ROS seen using superoxide-sensitive, Dihydroethidium (DHE, F); JNK signalling
772 visualized using a bio-sensor, TRE-dsRED, for JNK-mediated AP-1 signalling (G); DNA
773 double-strand breaks, marked by γH2AX (H), in *hsrω*^{66} and *hsrω*^{66}/+ counterpart and its
774 quantification on the right. The Y-axis of the graphs represents the fluorescence per ROI.

775 (I-K) Signatures of increased proteotoxicity in *hsrω*^{66} versus *hsrω*^{66}/+ wing epithelium:
776 Elevated LysoTracker fluorescence (I) and protein aggregates visualized using fluorescent
777 dye ProteoStat (J) in *hsrω*^{66} and *hsrω*^{66} /+ wing imaginal discs. Quantification of Thioflavin
778 fluorescence in cell homogenates of wing discs of *hsrω*^{66} and control larvae a measure of
779 protein aggregates.

780 Two-tailed Student's t-test was applied to determine the statistical significance between test
781 and controls in 2F-J; *$P \leq 0.05$ and **$P \leq 0.001$. Error bars represent mean ± SEM. ES:
782 Enrichment Score. p-value is the Nominal p-value. A negative value of NES indicates poor
783 enrichment of the queried geneset in *hsrω*^{66} mutant proteome versus control proteome. Scale
784 bars: 100 µm.

785

786 **Figure 3. Haploinsufficiency of *hsrω* is a tumor-permissive genetic background**

787 (**A**) GFP-marked *lgl*$^{-}$ somatic clones (GFP, green) induced using heat shock flippase,
788 generated in a wild type genetic background. *lgl* clones (*hsflp; lgl*^{4}*FRT40*) display cell death
789 (Caspase-3, red). Note enrichment of Caspase-positive *lgl* clones in basal compared to apical
790 projections of select optical sections on the right panel.

791 (**B-C**) *lgl*$^{-}$ somatic clones (GFP, green) in a heterozygous *hsrω*^{66}/+ background (*hsflp;*
792 *lgl*^{4}*FRT40; hsrω*^{66}/+) undergo neoplastic transformation revealed by disrupted F-Actin. Note
793 the characteristic large, dispersed nuclei (GFP) of transformed clones, and Caspase-3
794 expression along boundaries. Quantification of *lgl* clone area in wild type (WT) vs. *hsrω*^{66}/+
795 wing imaginal discs (C).

(**D-E**) *lgl*$^{-}$ clones in *hsrω*^{66}/+ imaginal discs displaying excessive proliferation (pH3, D) and elevated levels of Matrix Metalloproteinase (MMP1) expression (E).

(**F**) Graph displaying reduction in clone size of *lgl; hsrω*^{66}/+ tumors, when larvae were fed proteosome inhibitor MG-132 at two different concentrations.

(**G-I**) *lgl* somatic clones (marked in GFP) with co-down regulation *(hsflp; lgl*^{4} *UAS-hsrω-RNAi FRT40A* (G-I) or up regulation (*lgl*^{4} *FRT40A UAS-hsrω*^{EP3039}; J) of in *WT* genetic background. *lgl*$^{-}$ clones survive and undergo neoplastic transformation (stars), marked by disrupted F-Actin (Phalloidin staining) and induce exaggerated Caspase-3 expression along the clone boundary (G). Quantification of *lgl*$^{-}$ clone areas with loss (H) or gain (K) of *hsrω.*

Two-tailed Student's t-test was applied to determine the statistical significance between test and controls in 3C, F. H and K; *P≤ 0.05 and **P≤ 0.001. Scale bars: 100 µm.

Figure 4. Redox regulator *Keap1/Nrf2* and inflammatory gene *dSTING* are haploinsufficient for tumor suppression

(A-D) GFP-marked *lgl* somatic clones in a *Keap1* heterozygous genetic background (*lgl*^{4}*; Keap*^{EY5}/+, A), or upon cell autonomous downregulation of *Keap1* (*lgl*^{4}*; UAS-Keap1 RNAi*, B), or gain of downstream regulator CncC (*lgl*^{4}*; UAS-CncC,* C), display neoplastic transformation (disrupted F-Actin) and cell death along clone boundary (Caspase-3, C).

(E-F) GFP-marked *lgl* somatic clones in dSTING heterozygous (*lgl*^{4}*; STING*$^{\Delta RG5}$/+, E) or STING down regulated (*lgl*^{4}*; UAS-dSTING RNAi*, F) genetic background display neoplastic transformation with disrupted F-Actin.

(G-I) Disrupted sub-cellular distribution of dSTING in cells of *hsrω*^{66} mutant salivary gland (H) with enhanced punctae and reduced general cytoplasmic distribution compared with a uniform distribution and fewer punctae in wild type gland (G). (I) Representative wing discs from larvae bearing *lgl*$^{-}$ somatic tumors generated in *hsrω*^{66}/+ genetic background and fed on STING agonist, 2′3′-cGAMP, at two different concentrations; quantification of *lgl* clone size from unfed and fed larvae (far right).

Two-tailed Student's t-test was applied to determine the statistical significance between test and controls in 4I. NS: Not Significant.

Figure 5. Genetic variations in Sat III in human cancer patients

(A-B) Kaplan-Meier curves (generated on cBioPortal platform), comparing survival of individuals with epithelial cancer carrying Copy Number Alterations (CNA) in *HSF1* with individuals not carrying any alteration in *HSF1*. The y-axis represents the probability percent survival, and the x-axis shows progress free survival in months. The plot was generated by querying 91469 samples across 233 studies and included 16 cancer types, (A); Graph displaying the distribution of various genetic alterations in *HSF1* across patients (B).

833 (**C-E**) Schema depicting *Sat III* locus on pericentromeric region of chromosome 9 (C),
834 expression of *Sat III* in benign and prostate cancer cell lines (D). Violin plot depicting
835 germline copy number variations of *Sat III* in PCa patients compared to benign control, BPH
836 (E).

837 **Figure 6. Summary:**

838 Schema displaying haploinsufficiency as a strategy to uncover host genetic modifiers of
839 cancer susceptibility. Moderate genetic variations (haploinsufficiency) transform a tumor-
840 resistant wild type epithelium to a genetically altered tumor-permissive epithelium (right
841 panel).

842

843 **Supplementary data**

844 **Figure S1 Comparative Proteome of wing epithelium of *hsrω*^{66} mutants versus wild type**

845 **(A-B)** Box plot displaying abundance of proteins in *hsrω*^{66} mutant and wild type control
846 proteomes (A); Volcano plot of 3198 variables depicting the comparative levels of mis-
847 regulated proteins in *hsrω*^{66} proteome compared to wild type (B).

848 **(C-D)** Relative abundance ($\log_2$ fold change) of select proteins belonging to Protein
849 metabolism (C) and Stress response (D) functional classes in *hsrω*^{66} proteome compared to
850 its wild type counterpart.

851 **(E)** Rank-based Gene Ontology (GO) enrichment analysis of RNA polII transcription
852 regulatory complex (GO: 00905757) and Mediator complex. The x-axis represents the list of
853 proteins in ascending order of fold change in *hsrω*^{66} versus wild type wing disc proteome.
854 Black bars along the x-axis mark the position of proteins being queried. The tables alongside
855 give the protein levels of the top five mis-expressed proteins belonging to a given GO class.

856 (**F**) Representative examples of wing imaginal discs displaying increase in ubiquitinated
857 proteins using anti-Ubiquitin FK2 Antibody in *hsrω*^{66} and *hsrω*^{66}/+ wing imaginal discs.

858

859 **Figure S2. *lgl* clones display cellular stress**

860 **(A-C)** GFP-marked *lgl* mutant cells generated in a wild type epithelia exhibit signatures of
861 cellular stress. *lgl* clones (GFP, green) display elevated levels of ROS, (DHE, Red, A),
862 increase in MitoTracker staining, revealing perturbed mitochondrial activity (B), and elevated
863 number of acidic lysosomes as seen by LysoTracker staining (red, C). Area marked by yellow
864 box magnified on the right in each case. Scale bars: 100 µm.

865 **Figure S3. Genetic disruption of omega biocondensates facilitates *lgl* tumor progression**

866 **(A-B)** GFP-marked *lgl* clones generated in *Df(3R)Hrb87F/+* genetic background
867 (*lgl;Df(3R)Hrb87F/+,* A) or with co-downregulation of ISWI (*lgl;UAS-ISWI-RNAi,*) undergo

868 neoplastic transformation, as revealed by disrupted F-Actin. Transformed clones exhibit loss
869 of junction protein FasIII (**A**). Scale bars: 100 µm.

870 **Figure S4 *hsrω*/+ host genetic background facilitates growth of *lgl* tumors in *Drosophila***
871 **adult gut**

872 (**A-C**) GFP-marked somatic control (wild type) (A) or with loss of *lgl* (B, C) clones generated
873 in wild type (A, B) or $hsr\omega^{66}$/+ (C) genetic background. Note significantly large *lgl* clones in
874 C compared to A or B, with characteristic small nuclei (red, stained with To-PRO) indicative
875 of intestinal stem cells.

876 **Figure S5. Cellular Localization of STING**

877 **(A)** Uniform punctae of dSTING in cells of larval salivary gland over expressing dSTING (*vg*
878 *Gal4 >UAS-dSTING*).

879 **Figure S6. Genetic variations in *Sat III* in human cancer patients**

880 **(A-B)** Kaplan-Meier survival curves generated on cBioPortal (cbioportal.org): comparing
881 survival of individuals with epithelial cancer carrying Copy Number Alterations (CNA) in
882 *KEAP1* with individuals not carrying an alteration in *KEAP1*. The plot was generated by
883 querying 91469 samples across 233 studies, across 16 cancer types (A). The inset displays
884 distribution of various genetic alterations in *HSF1* across patients (B); comparing survival of
885 individuals with cancers of Lymphoid origin, carrying Copy Number Alterations (CNA) in
886 *STING1*. The plot was generated by querying 9672 samples across 17 studies.

887

888

Figure 1

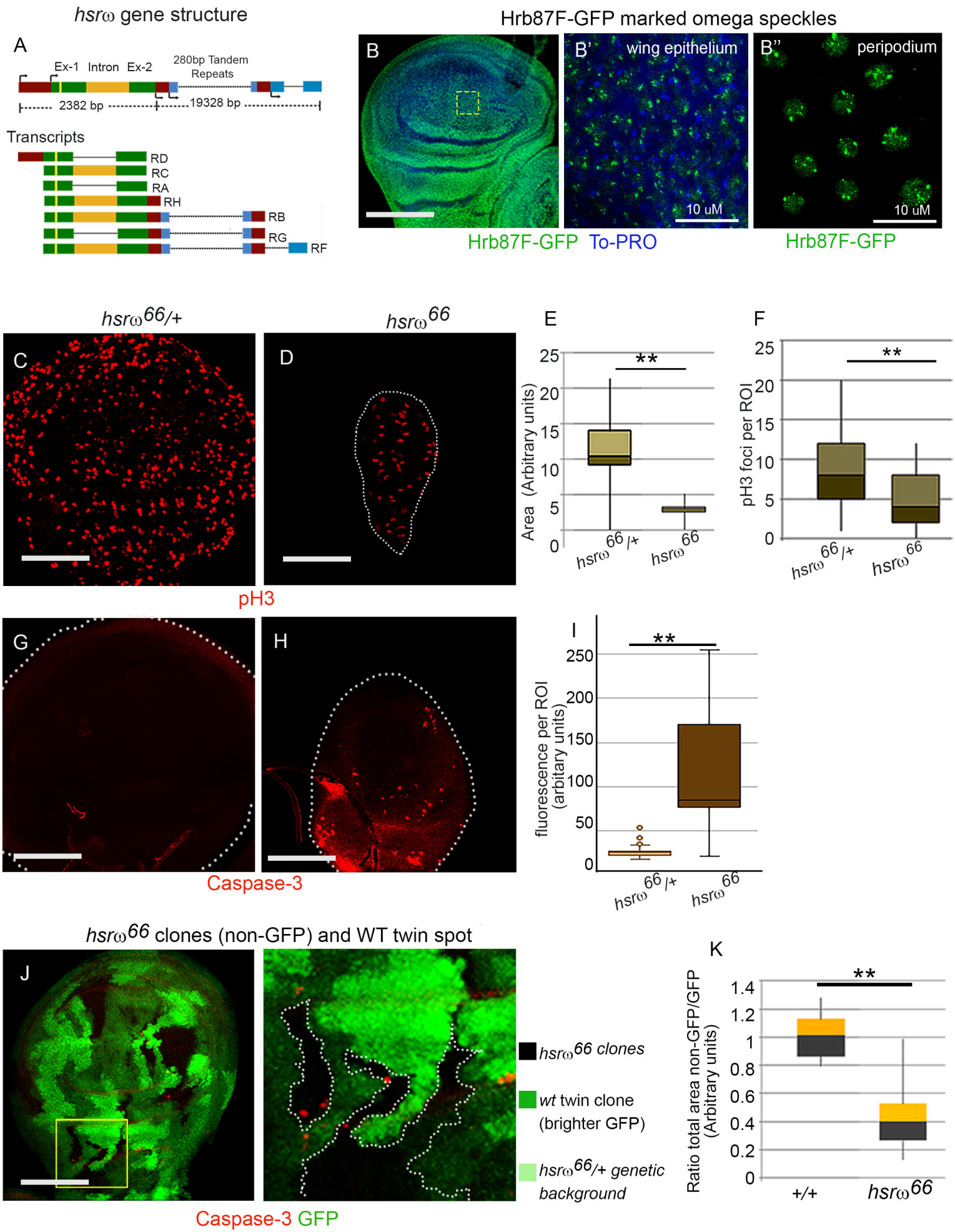
hsrω gene structure
A
Ex-1
Intron
Ex-2
280bp Tandem Repeats
2382 bp
19328 bp
Transcripts
RD
RC
RA
RH
RB
RG
RF
Hrb87F-GFP marked omega speckles
B
B'
wing epithelium
B''
peripodium
10 uM
10 uM
Hrb87F-GFP To-PRO
Hrb87F-GFP
hsrω66/+
hsrω66
C
D
pH3
E
Area (Arbitrary units)
**
hsrω66/+
hsrω66
F
pH3 foci per ROI
**
hsrω66/+
hsrω66
G
H
Caspase-3
I
fluorescence per ROI (arbitary units)
**
hsrω66/+
hsrω66
hsrω66 clones (non-GFP) and WT twin spot
J
Caspase-3 GFP
hsrω66 clones
wt twin clone (brighter GFP)
hsrω66/+ genetic background
K
Ratio total area non-GFP/GFP (Arbitrary units)
**
+/+
hsrω66

Figure 2

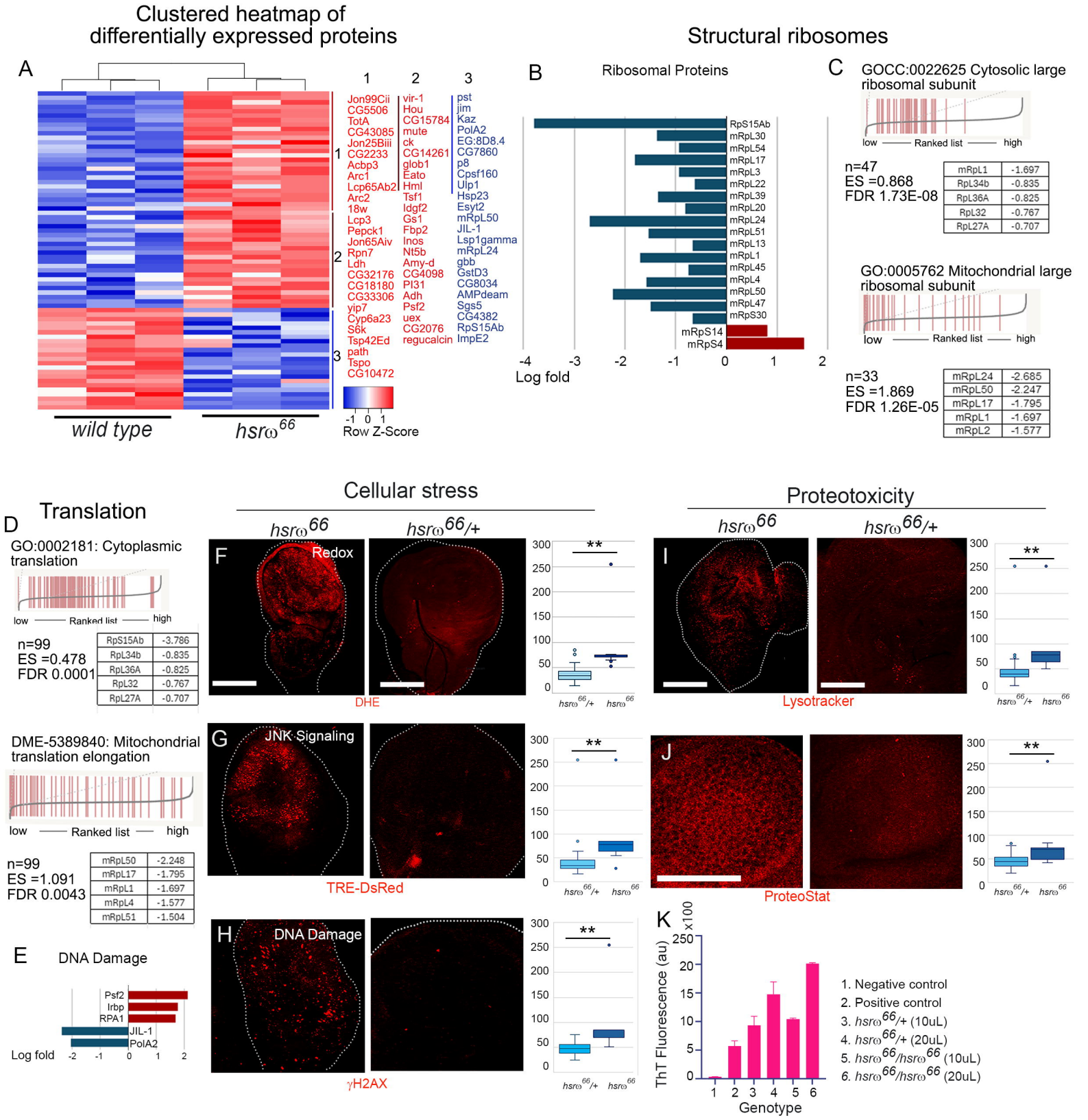
Clustered heatmap of differentially expressed proteins
A
1 2 3
Jon99Cii CG5506 TotA CG43085 Jon25Biii CG2233 Acbp3 Arc1 Lcp65Ab2 Arc2 18w
Lcp3 Pepck1 Jon65Aiv Rpn7 Ldh CG32176 CG18180 CG33306 yip7 Cyp6a23 S6k Tsp42Ed path Tspo CG10472
vir-1 Hou CG15784 mute ck CG14261 glob1 Eato Hml Tsf1 Idgf2 Gs1 Fbp2 Inos Nt5b Amy-d CG4098 PI31 Adh Psf2 uex CG2076 regucalcin
pst jim Kaz PolA2 EG:8D8.4 CG7860 p8 Cpsf160 Ulp1 Hsp23 Esyt2 mRpL50 JIL-1 Lsp1gamma mRpL24 gbb GstD3 CG8034 AMPdeam Sgs5 CG4382 RpS15Ab ImpE2
wild type
hsrω66
-1 0 1
Row Z-Score
Structural ribosomes
B
Ribosomal Proteins
RpS15Ab mRpL30 mRpL54 mRpL17 mRpL3 mRpL22 mRpL39 mRpL20 mRpL24 mRpL51 mRpL13 mRpL1 mRpL45 mRpL4 mRpL50 mRpL47 mRpS30 mRpS14 mRpS4
-4 -3 -2 -1 0 1 2
Log fold
C
GOCC:0022625 Cytosolic large ribosomal subunit
low Ranked list high
n=47
ES =0.868
FDR 1.73E-08
mRpL1 -1.697
RpL34b -0.835
RpL36A -0.825
RpL32 -0.767
RpL27A -0.707
GO:0005762 Mitochondrial large ribosomal subunit
low Ranked list high
n=33
ES =1.869
FDR 1.26E-05
mRpL24 -2.685
mRpL50 -2.247
mRpL17 -1.795
mRpL1 -1.697
mRpL2 -1.577
D
Translation
GO:0002181: Cytoplasmic translation
low Ranked list high
n=99
ES =0.478
FDR 0.0001
RpS15Ab -3.786
RpL34b -0.835
RpL36A -0.825
RpL32 -0.767
RpL27A -0.707
DME-5389840: Mitochondrial translation elongation
low Ranked list high
n=99
ES =1.091
FDR 0.0043
mRpL50 -2.248
mRpL17 -1.795
mRpL1 -1.697
mRpL4 -1.577
mRpL51 -1.504
E
DNA Damage
Psf2 Irbp RPA1 JIL-1 PolA2
Log fold -2 -1 0 1 2
Cellular stress
hsrω66 hsrω66/+
F Redox
DHE
G JNK Signaling
TRE-DsRed
H DNA Damage
γH2AX
Proteotoxicity
hsrω66 hsrω66/+
I
Lysotracker
J
ProteoStat
300 250 200 150 100 50 0
**
hsrω66/+ hsrω66
K
ThT Fluorescence (au) x100
250 20 15 10 5 0
1 2 3 4 5 6
Genotype
1. Negative control
2. Positive control
3. hsrω66/+ (10uL)
4. hsrω66/+ (20uL)
5. hsrω66/hsrω66 (10uL)
6. hsrω66/hsrω66 (20uL)

Figure 3

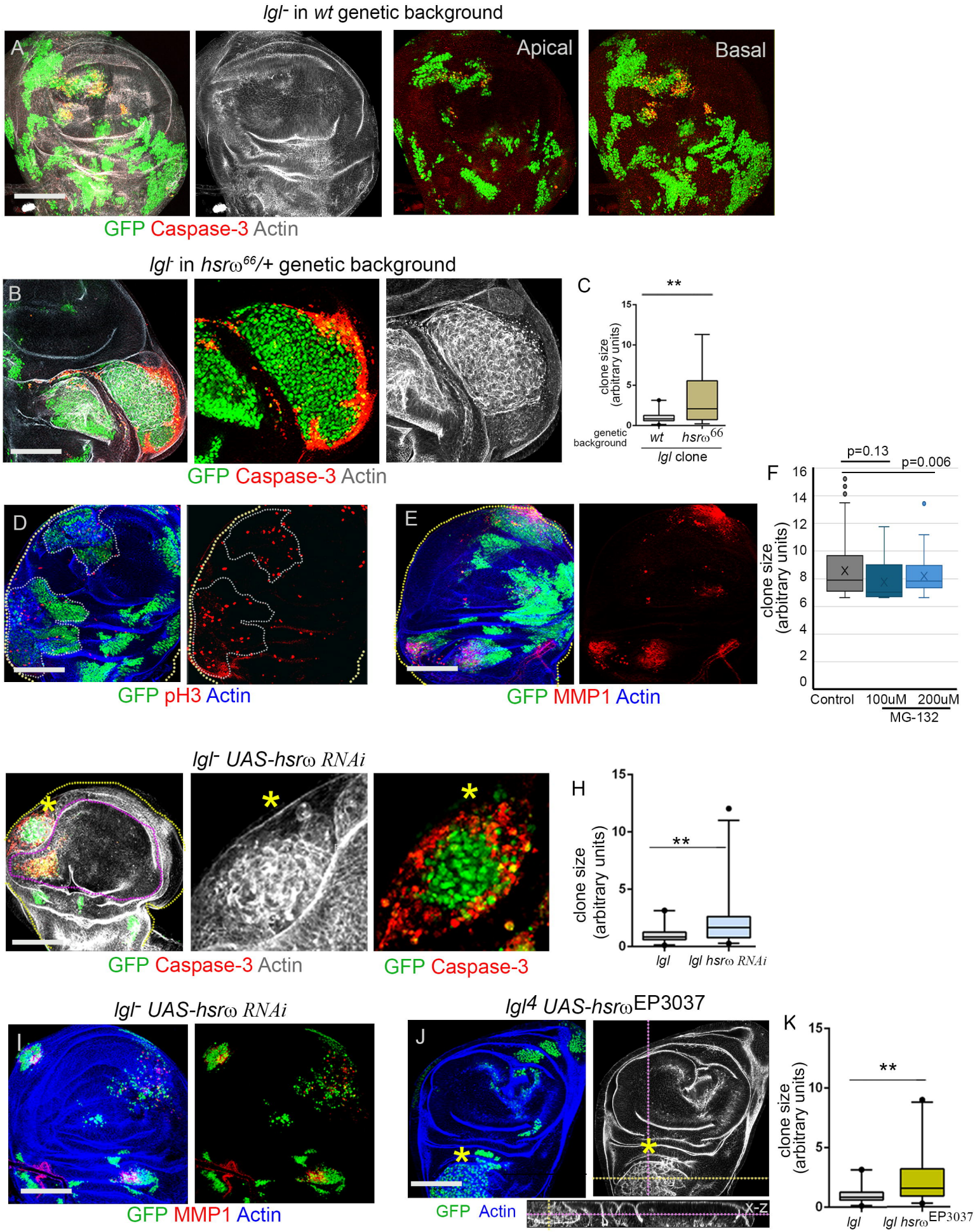
lgl- in wt genetic background
A
Apical
Basal
GFP Caspase-3 Actin
lgl- in hsrω66/+ genetic background
B
C
**
clone size (arbitrary units)
genetic background
wt
hsrω66
lgl clone
GFP Caspase-3 Actin
D
E
GFP pH3 Actin
GFP MMP1 Actin
F
p=0.13
p=0.006
clone size (arbitrary units)
Control
100uM
200uM
MG-132
lgl- UAS-hsrω RNAi
GFP Caspase-3 Actin
GFP Caspase-3
H
**
clone size (arbitrary units)
lgl
lgl hsrω RNAi
lgl- UAS-hsrω RNAi
I
GFP MMP1 Actin
lgl4 UAS-hsrωEP3037
J
GFP Actin
X-Z
K
**
clone size (arbitrary units)
lgl
lgl hsrωEP3037

Figure 4

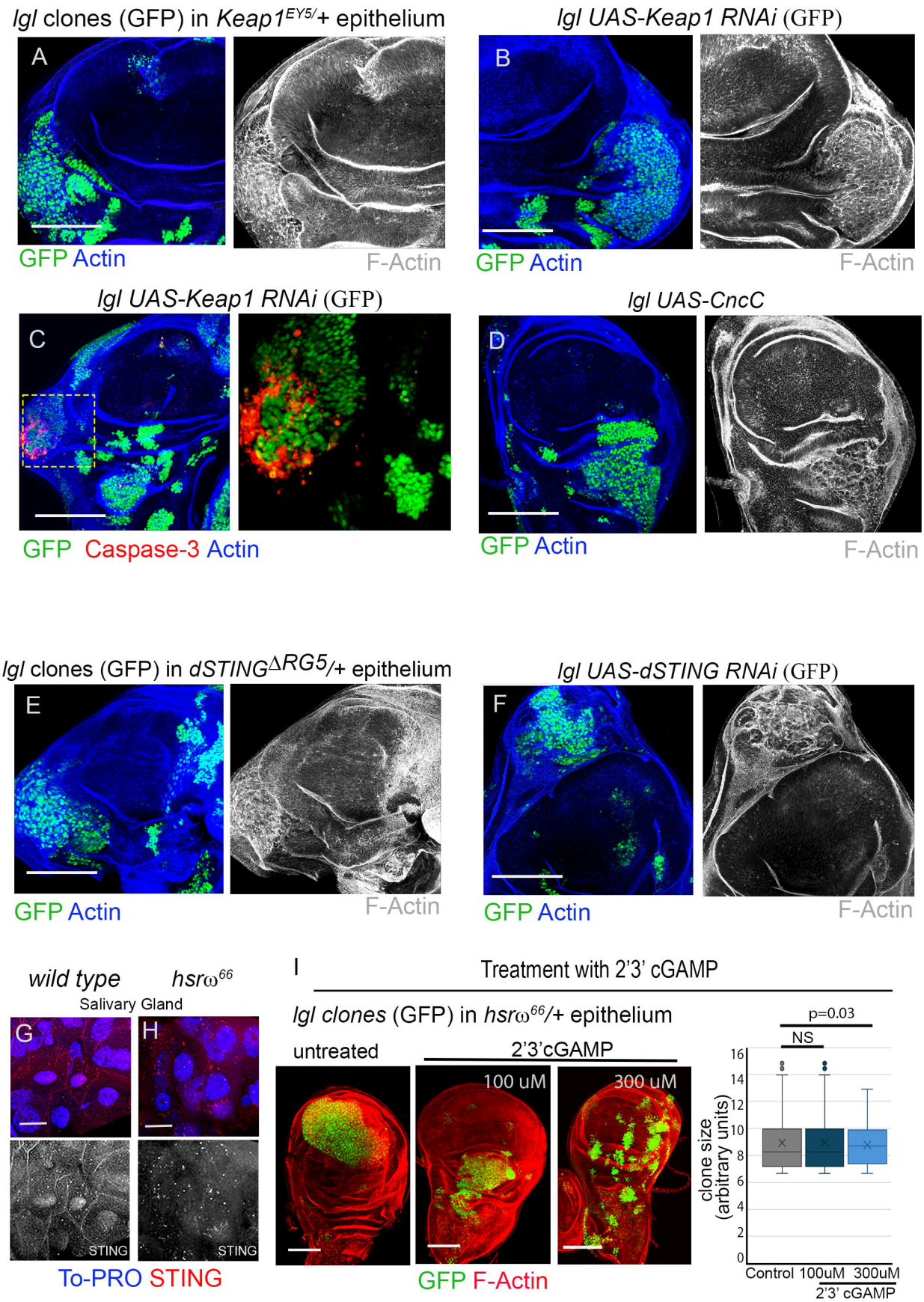
lgl clones (GFP) in Keap1EY5/+ epithelium
A
GFP Actin
F-Actin
lgl UAS-Keap1 RNAi (GFP)
B
GFP Actin
F-Actin
lgl UAS-Keap1 RNAi (GFP)
C
GFP Caspase-3 Actin
lgl UAS-CncC
D
GFP Actin
F-Actin
lgl clones (GFP) in dSTINGΔRG5/+ epithelium
E
GFP Actin
F-Actin
lgl UAS-dSTING RNAi (GFP)
F
GFP Actin
F-Actin
wild type
hsrω66
Salivary Gland
G
H
STING
STING
To-PRO STING
I
Treatment with 2'3' cGAMP
lgl clones (GFP) in hsrω66/+ epithelium
untreated
2'3'cGAMP
100 uM
300 uM
GFP F-Actin
p=0.03
NS
clone size (arbitrary units)
16
14
12
10
8
6
4
2
0
Control 100uM 300uM
2'3' cGAMP

Figure 5

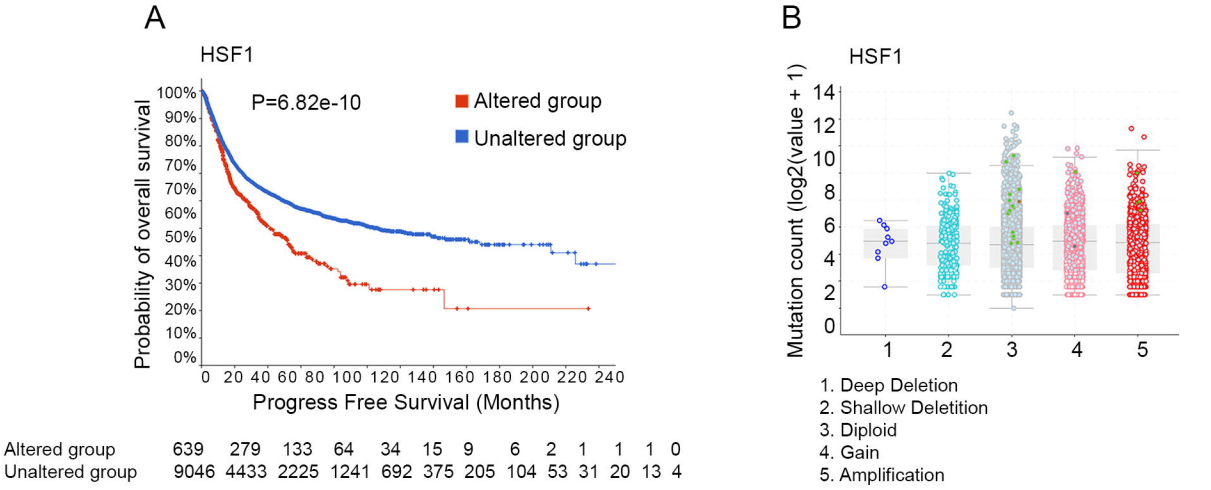
A
HSF1
P=6.82e-10
Altered group
Unaltered group
Probability of overall survival
100%
90%
80%
70%
70%
60%
50%
40%
30%
20%
10%
0%
0 20 40 60 80 100 120 140 160 180 200 220 240
Progress Free Survival (Months)
Altered group 639 279 133 64 34 15 9 6 2 1 1 1 0
Unaltered group 9046 4433 2225 1241 692 375 205 104 53 31 20 13 4
B
HSF1
Mutation count (log2(value + 1))
14
12
10
8
6
4
2
0
1 2 3 4 5
1. Deep Deletion
2. Shallow Deletition
3. Diploid
4. Gain
5. Amplification
C
9q11-q12
D
Germline copy number variations in Sat III
P=0.01
SatIII copies/µl
250
200
150
100
50
0
BPH(n=5) PCa(n=18)
E
Expression of Sat III in human cancer cell lines
Log10 SatIII/GAPDH expression
10000
1000
100
10
1
PNT2
22RV1
PC3
VCaP
LNCaP

Figure 7

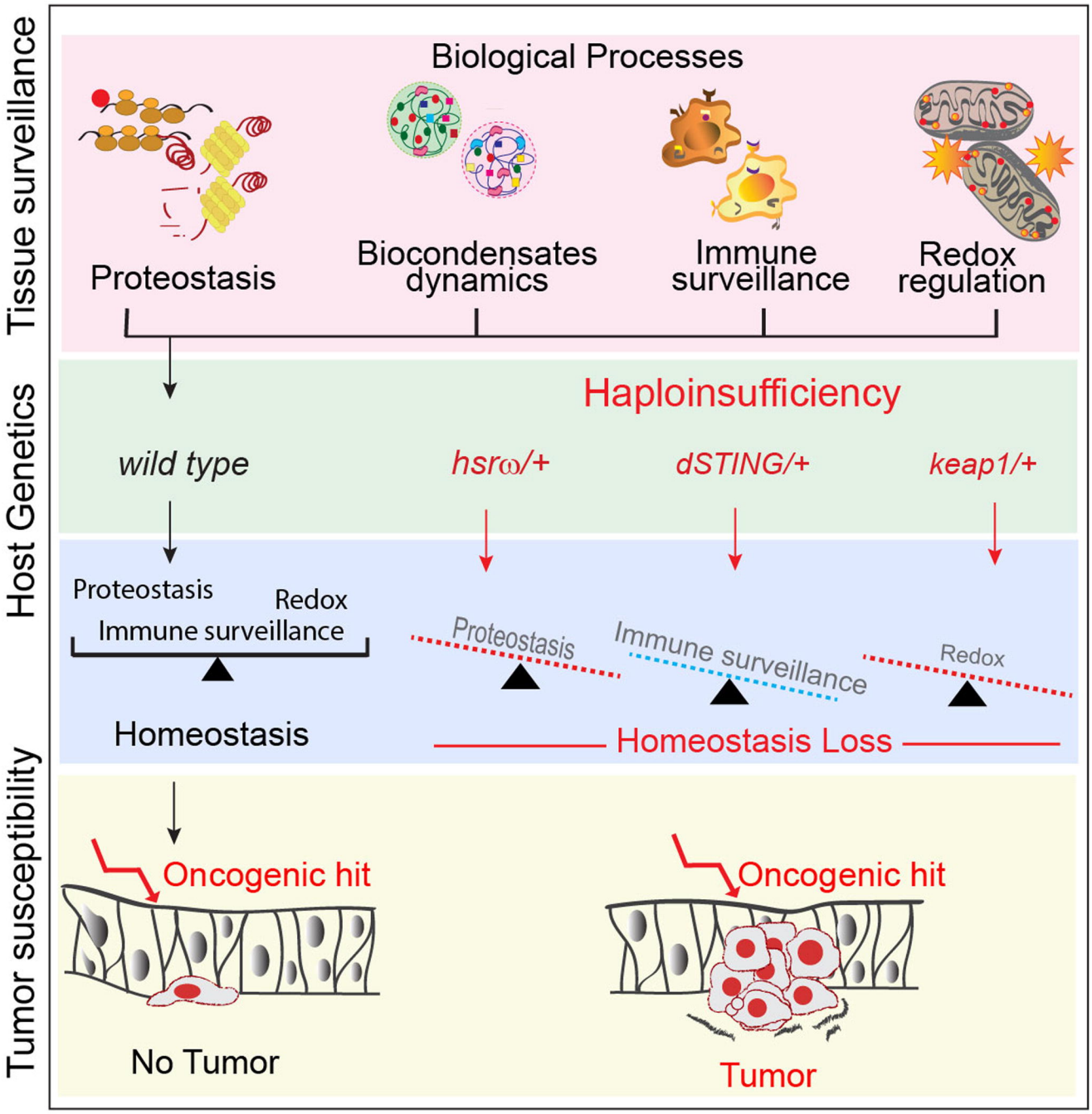
Tissue surveillance
Host Genetics
Tumor susceptibility
Biological Processes
Proteostasis
Biocondensates dynamics
Immune surveillance
Redox regulation
Haploinsufficiency
wild type
hsrω/+
dSTING/+
keap1/+
Proteostasis
Redox
Immune surveillance
Homeostasis
Proteostasis
Immune surveillance
Redox
Homeostasis Loss
Oncogenic hit
No Tumor
Oncogenic hit
Tumor